Fischer, R. A., Campbell, A. J., Shofner, G. A., Lord, O. T., Dera, P., & Prakapenka, V. B. (2011). Equation of state and phase diagram of FeO. *Earth and Planetary Science Letters*, *304*(3-4), 496-502. https://doi.org/10.1016/j.epsl.2011.02.025

Equation of state and phase diagram of FeO

Rebecca A. Fischer[a,*,1], Andrew J. Campbell[a,1], Gregory A. Shofner[a], Oliver T. Lord[b,2], Przemyslaw Dera[c], and Vitali B. Prakapenka[c]

[a]Department of Geology, University of Maryland, College Park, MD 20742, USA

[b]Department of Earth Sciences, University of Bristol, Wills Memorial Building, Queen's Road, Bristol, BS81RJ, UK

[c]Center forAdvanced Radiation Sources, 9700 South Cass Avenue, Building 434A, Argonne, IL 60439, USA

[*]Corresponding author. Email: rfischer@uchicago.edu. Phone: (773) 834-1085. Fax: (773) 702-9505

[1]Present address: Department of the Geophysical Sciences, University of Chicago, 5734 South Ellis Avenue, Chicago, Illinois 60637, USA

[2]Present address: Department of Earth Sciences, University College London, Gower Street, London, WC1E 6BT, UK

Abstract

Wüstite, $Fe_{1-x}O$, is an important component in the mineralogy of Earth's lower mantle and may also be a component in the core. Therefore the high pressure, high temperature behavior of FeO, including its phase diagram and equation of state, is

essential knowledge for understanding the properties and evolution of Earth's deep interior. We performed X-ray diffraction measurements using a laser-heated diamond anvil cell to achieve simultaneous high pressures and temperatures. Wüstite was mixed with iron metal, which served as our pressure standard, under the assumption that negligible oxygen dissolved into the iron. Our data show a positive slope for the subsolidus phase boundary between the B1 and B8 structures, indicating that the B1 phase is stable at the *P-T* conditions of the lower mantle and core. We have determined the thermal equation of state of B1 FeO to 156 GPa and 3100 K, finding an isothermal bulk modulus $K_0 = 149.4 \pm 1.0$ GPa and its pressure derivative $K_0' = 3.60 \pm 0.4$. This implies that 7.7 ± 1.1 weight percent oxygen is required in the outer core to match the seismologically-determined density, under the simplifying assumption of a purely Fe-O outer core.

Keywords: wüstite; high pressure; equations of state; phase equilibria; oxygen fugacity

1. Introduction

Wüstite, $Fe_{1-x}O$, is an important endmember of (Mg,Fe)O in the Earth's lower mantle and possibly also a significant alloying component of the core (McDonough, 2003). Iron is the most abundant multivalent element in the mantle; its oxidation state dominates the redox chemistry of the mantle, in turn controlling element partitioning, phase equilibria, diffusion, and related physical and chemical properties (Frost and

McCammon, 2008). If oxygen is a primary light element component in the core, then its impact on the density of Fe-rich melts is critical to interpreting the composition, dynamics, and evolution of the core. Therefore it is essential to understand the high pressure, high temperature phase relations and thermodynamics of the Fe-O system. In this study we focus on the thermal equation of state and subsolidus phase diagram of stoichiometric iron oxide, FeO.

Under ambient conditions wüstite is stable in the B1 (NaCl-type) crystal structure. With room temperature compression it undergoes a rhombohedral $R\bar{3}$ (Mao et al., 1996) distortion around 17 GPa, with the transition pressure depending on the degree of hydrostaticity (Fei, 1996; Fei and Mao, 1994). This distortion has also been reported to be to a monoclinic *C*2/*m* phase, both at high pressures (Kantor et al., 2008) and at 1 bar and low temperatures (Fjellvåg et al., 2002). Diamond cell and shock wave experiments show a transformation of wüstite to the B8 (NiAs-type) crystal structure at high pressures and temperatures (Fei and Mao, 1994; Jeanloz and Ahrens, 1980; Knittle and Jeanloz, 1991; Kondo et al., 2004; Murakami et al., 2004; Ozawa et al., 2010; Yagi et al., 1988), based on X-ray diffraction and electrical resistivity measurements. However, the location and slope of the B1/B8 transition is inconsistent among these studies, with some reporting a vertical slope around 70 GPa at high temperatures (Knittle and Jeanloz, 1991; Murakami et al., 2004; Yagi et al., 1988) and others indicating a strongly positive slope in pressure-temperature space (Kondo et al., 2004; Ozawa et al., 2010). Some investigators have failed to observe the transition to the B8 phase altogether (Mao et al., 1996; Sata et al., 2005; Seagle et al., 2008; Yagi et al., 1985), and have attributed this to differences in stoichiometry (Seagle et al., 2008) or kinetic barriers at room temperature

(Mao et al., 1996). The melting curve of $Fe_{1-x}O$ has been determined up to pressures and temperatures of 77 GPa and 3100 K (Fischer and Campbell, 2010), with reasonable agreement between multi-anvil press (Ringwood and Hibberson, 1990) and diamond anvil cell experiments (Boehler, 1992; Fischer and Campbell, 2010; Shen et al., 1993).

The thermal equation of state of FeO is important for interpreting the seismological structure of the Earth's lower mantle and the density deficit, relative to pure iron, of Earth's outer core. Room temperature studies have shown that the degree of nonstoichiometry in wüstite does not significantly affect its bulk modulus (Fei, 1996), although some ambiguity remains (Mao et al., 1996; McCammon, 1993). The equation of state and high pressure phase transition in wüstite has also been studied by shock compression (Jeanloz and Ahrens, 1980; Yagi et al., 1988). A recent static compression study expanded the equation of state of FeO to high temperatures, where the B1 (non-distorted) phase is stable to much higher pressure (Campbell et al., 2009); this yielded an isothermal bulk modulus $K_0 = 146.9$ GPa with a fixed pressure derivative $K_0' = 4$.

In this study, we aim to constrain the B1/B8 phase boundary of FeO using X-ray diffraction in a laser-heated diamond anvil cell, to resolve between existing discrepancies in the literature data. We also aim to determine the thermal equation of state of B1 FeO at higher pressures and temperatures than previous studies (Campbell et al., 2009), extending the existing dataset into the *P*-*T* region of the outer core. This will allow for calculations of the amount of oxygen required to match the observed density deficit in the outer core, and also improved understanding of the iron-iron oxide oxygen fugacity buffer at core conditions, with minimal extrapolation required over pressure and temperature.

2. Experimental Methods

The equation of state of FeO was determined by measuring its lattice parameter using synchrotron X-ray diffraction during laser-heating in a diamond anvil cell. The FeO was mixed with metallic Fe to ensure that the oxide was saturated in iron, and presumably stoichiometric, at high pressures and temperatures (Campbell et al., 2009; Seagle et al., 2008; Stølen and Grønvold, 1996). Seagle et al. (2008) laser heated wüstite+Fe mixtures up to 93 GPa and found the recovered samples to be stoichiometric; we assume a similar equilibration took place in our higher pressure sample, but this could not be verified directly because the anvils broke before decompression and the sample was destroyed.

Sample material was prepared by mixing $Fe_{0.94}O$ powder (a = 4.302 ± 0.001 Å; McCammon and Liu, 1984) with Fe powder in a ratio of 1:1.23 by mass, which produces a ~10 wt% oxygen content in the mixture. The mixture was mechanically ground under ethanol to a grain size of ~1 μm, then dried in an oven at 85°C for one hour. The powder was pressed in a diamond anvil cell to form a foil approximately 70 μm in diameter and 5 μm thick. A rhenium gasket, initially 250 μm thick, was preindented to ~27 GPa, and a hole 80 μm in diameter in the center of the indentation served as the sample chamber. Beveled diamond anvils were used, with 150 μm flats and an 8° bevel out to 300 μm. The sample was loaded between two layers of NaCl ~10 μm thick, which acted as the

115 pressure medium and thermal insulator. The sample assembly was oven-dried at 85°C for
116 one hour after cell loading but before pressurization.
117 Angle-dispersive X-ray diffraction experiments were performed at beamline 13-
118 ID-D (GeoSoilEnviroCars) of the Advanced Photon Source, Argonne National
119 Laboratory (Prakapenka et al., 2008; Shen et al., 2005). The incident X-ray beam was
120 monochromatic (λ = 0.3344 Å) and measured 5 μm x 5 μm. Diffracted X-rays were
121 recorded using a MAR165 CCD detector, with the sample-to-detector distance calibrated
122 by 1 bar diffraction of CeO_2. Exposure times were typically 5 s.
123 The X-ray diffraction patterns were integrated to produce two-theta plots using
124 Fit2D (Hammersley et al. 2006). Peak fitting of the integrated patterns was performed
125 using PeakFit (Systat Software). Overlapping peaks were deconvoluted in nearly all
126 cases. Overlapped peaks that could not be deconvoluted were not used, except in a small
127 number of cases when necessary to constrain the uncertainty for a hexagonal phase, and
128 when their use or exclusion did not change the calculated lattice parameter within error.
129 Pressures were determined from the volume of hcp-iron, using the thermal equation of
130 state of Dewaele et al. (2006). This equation of state was calibrated against both room
131 temperature and shock wave compression to >200 GPa, and includes an explicit,
132 theoretically derived electronic contribution. Uncertainties in pressure were calculated
133 based on the uncertainty in temperature and the uncertainty in the lattice parameters of
134 hcp-iron, which were determined from four to seven d-spacings.
135 Our calculation of pressure is based on the unit cell volume of iron and the
136 temperature of the sample, corrected for an axial temperature gradient (Campbell et al.,
137 2007). In using iron as the pressure standard, we are assuming both mechanical and

thermal equilibrium between the Fe and FeO, which were intimately mixed (Campbell et al., 2009). Deviatoric stresses on the sample are expected to be negligible, as are compositional inhomogeneities that might place the pressure standard and the sample material under slightly different *P-T* conditions. We are also assuming that there is no dissolved oxygen in the iron that is altering its unit cell volume, which is supported by an earlier study of recovered Fe+FeO samples (Ozawa et al., 2010).

The sample was compressed to a target pressure and laser-heated from each side by 1.064 μm Yb fiber lasers with 'flat top' profiles created by Pi-shaping optics, with the laser power on each side being independently adjustable (Prakapenka et al., 2008). The temperature was slowly stepped up by increasing the laser power until a target temperature was reached, and then the laser power was decreased gradually to zero, with diffraction patterns being obtained both on heating and cooling cycles. Temperatures were determined spectroradiometrically (Heinz and Jeanloz, 1987) using the graybody approximation over the 600-800 nm range of thermal emission, and were measured during the collection of each diffraction pattern. The laser-heated spots were ~20-25 μm in diameter, much larger than the X-ray beam to minimize radial temperature gradients, and were coaligned with the beam using X-ray induced fluorescence from the NaCl insulator. Upstream and downstream laser powers were adjusted during heating to equalize the intensity of the thermal emission on the two surfaces of the sample. All temperature measurements used in this study were recorded on the upstream side of the sample, because of technical difficulties with measurements on the downstream side during this set of experiments. Temperatures were measured from a region 5 μm in

diameter in the center of the laser-heated spot, comparable in size to the area probed by the X-rays.

Temperatures measured on the surface of the sample were corrected downward by 3% to account for an axial temperature gradient through the thickness of the sample, based on a sample thickness of ~5 μm (Campbell et al., 2007, 2009). Reported uncertainties in temperature incorporate an analytical uncertainty of 100 K (Shen et al., 2001), as well as the uncertainty from the correction for the axial temperature gradient (Campbell et al., 2007, 2009).

To verify the accuracy of the temperature measurements, a sample of pure iron loaded in an MgO pressure medium was analyzed to check the location of the hcp-fcc phase transition in iron. The sample was pressurized to 36.4 ± 0.5 GPa before heating, based on the lattice parameter of hcp-Fe (Dewaele et al., 2006). The phase transition in iron was bracketed between volumes and temperatures of 6.014 ± 0.006 cm^3/mol, 1563 ± 107 K (hcp-Fe) and 6.140 ± 0.080 cm^3/mol, 1609 ± 108 K (fcc-Fe) on heating, which agrees with the published phase diagram of Komabayashi and Fei (2010).

3. Results

The pressure-volume-temperature (*P*-*V*-*T*) data from the synchrotron X-ray diffraction experiments are listed in Table S1 of the Supplementary Material. The lattice parameters of hcp-Fe were calculated from four to seven of the following peaks: 100, 002, 101, 102, 110, 103, 112. The lattice parameter of B1-FeO was determined from

three to six of the following peaks: 111, 200, 220, 311, 222, 400, 331, and those of B8-FeO were calculated from up to four of the following peaks: 002, 100, 101, 102, 112, 104, 202. A unit cell volume for B8-FeO is only reported when at least two non-overlapping peaks were observed. In addition, the lattice parameter of B2-NaCl was determined from the observed *d*-spacings of three to six of the following *hkl* peaks: 100, 110, 111, 200, 211, 220. Figure 1a and b shows a diffraction pattern collected at 144 GPa and 3025 K with peaks corresponding to B2-NaCl, B1-FeO, and hcp-Fe, while Figure 1c shows a pattern collected at 151 GPa and 1665 K with peaks corresponding to B2-NaCl, B8-FeO, and hcp-Fe.

Figure 2 illustrates the comparison of our B1-FeO *P-V-T* data with those of Seagle et al. (2008), Campbell et al. (2009), and Ozawa et al. (2010), which were all synchrotron X-ray diffraction studies of wüstite coexisting with metallic iron. All of these data were obtained using a laser-heated diamond anvil cell, except for the data up to ~10 GPa from Campbell et al. (2009), which were obtained in a multi-anvil press. This study and Ozawa et al. (2010) report pressures based on the unit cell volume of hcp-Fe (Dewaele et al., 2006); for comparison, the pressures of the Seagle et al. (2008) and Campbell et al. (2009) data have been recalculated based on the unit cell volume of iron, using the equation of state of hcp-Fe (Dewaele et al., 2006) or fcc-Fe (Campbell et al., 2009). These studies had originally reported pressures based on the unit cell volume of B1- or B2-NaCl; the difference in calculated pressure between the NaCl and Fe pressure standards for those data is 0.3%, on average.

Figure 3 shows our B8-FeO *P-V-T* data and those of Ozawa et al. (2010). Also shown for comparison are the lone data point from Kondo et al. (2004), who studied

206 $Fe_{0.95}O$ using ruby fluorescence to measure the pressure (Mao et al., 1978), and the lone
207 data point from Fei and Mao (1994), who studied $Fe_{0.98}O$ and used the equation of state
208 of gold (Anderson et al., 1989) to calculate the pressure.
209 Figure 4 shows the phase diagram of FeO. The B1 and B8 phases of FeO were
210 frequently seen to coexist in these experiments. Presumably this is hysteresis from the
211 kinetics of the transformation, as well as a contribution from the aforementioned thermal
212 gradients in the laser-heated sample. We determined the phase boundary by monitoring
213 the growth in relative intensities of several peaks in each phase. For example, *P*-*T*
214 conditions in which the B1 peak intensities were increasing and the B8 peak intensities
215 were decreasing relative to the previous X-ray diffraction pattern were assigned to the B1
216 stability field (Kondo et al., 2004; Murakami et al., 2010).
217
218
219 **4. Discussion**
220
221 *4.1. B1/B8 phase transition*
222 The B1/B8 phase boundary observed in this study is broadly consistent with that
223 of Kondo et al. (2004), but at slightly lower temperatures than would be expected from
224 the results of Ozawa et al. (2010) (Figure 4). The disagreement between these datasets
225 could be due to the large uncertainties in temperature reported by Ozawa et al. (2010);
226 otherwise, the high degree of curvature required for a phase boundary to match both of
227 those datasets, in addition to the present results, is unlikely. Our data are incompatible
228 with the phase boundaries of Fei and Mao (1994), but it is important to note that we

measured the B1/B8 transition, while they measured the rhombohedral/B8 transition, at temperatures far from the triple point. However, any B1/B8/rhombohedral triple point based on our data and those of Fei and Mao (1994) would be in violation of Schreinemaker's rules (Zen, 1966), because of the angles between the phase boundaries at the B1/B8/rhombohedral triple point that are required by the combination of our data with those of Fei and Mao (1994) (Figure 4). One or more additional phase boundaries could also resolve these apparent disagreements in the phase diagram of wüstite, but no such transitions were detected in this study.

Our B1/B8 transition matches the shock wave results of Jeanloz and Ahrens (1980) within the large uncertainty of their temperature measurement, but it is inconsistent with the high-pressure phase transition reported by Knittle and Jeanloz (1991). Knittle and Jeanloz (1991) did not obtain any structural information, so their results could correspond to an electronic transition that is distinct from the B1/B8 transition.

Regardless of these small inconsistencies between various studies, our phase diagram confirms the conclusion of Ozawa et al. (2010) that it is the B1 structure of FeO, not the B8 structure, that is stable under the *P*-*T* conditions relevant to the Earth's lower mantle and outer core. Therefore, it is the equation of state of B1-FeO that we apply to calculations of the core density deficit and oxygen fugacity buffers (Sections 4.3 and 4.4).

4.2. Equations of state

Our new higher-pressure *P*-*V*-*T* data on B1-FeO are not precisely described by an extrapolation of the equation of state of Campbell et al. (2009), with the extrapolated

252 equation of state predicting pressures in excess of 5 GPa higher than those measured.
253 Therefore, we have redetermined the equation of state of B1-FeO, expanding the dataset
254 used by Campbell et al. (2009) with the addition of higher *P-T* data from this study and
255 from Ozawa et al. (2010), which allows us to fit more parameters in the equation of state.
256 We have also constructed an equation of state for B8-FeO, which had not previously been
257 determined for iron-saturated wüstite.

258 We fit *P-V-T* datasets of B1- and B8-FeO to Mie-Grüneisen equations of state,

259 $$P = P_{300}(V) + (\gamma/V)[E(\theta_D,T) - E_{300}(\theta_D,300)] \quad (1)$$

260 with the 300 K isothermal pressure (P_{300}) described by a third-order Birch-Murnaghan
261 equation of state (Birch, 1952) and the thermal pressure term based on a Debye model of
262 vibrational energy (E), with Grüneisen parameter $\gamma = \gamma_0(V/V_0)^q$ and Debye temperature θ_D
263 $= \theta_0 * \exp[\gamma_0/q*(1 - (V/V_0)^q)]$. We did not explicitly include any anharmonic or electronic
264 contributions to the thermal pressure. This reduced the number of fitted parameters,
265 which was necessary given the resolution of our data.

266 The equation of state parameters for B1- and B8-FeO are listed in Table 1. For
267 B1-FeO, we fit the present data along with those of several previous studies (Campbell et
268 al., 2009; Ozawa et al., 2010; Seagle et al., 2008). We fixed the parameters V_0
269 (McCammon and Liu, 1984), θ_0 (Stixrude and Lithgow-Bertelloni, 2007), and q, finding
270 a good fit to the data for $q = 0.5$. Our fitted values of K_0 and K_0' (149.4 GPa and 3.60,
271 respectively) show excellent agreement with the trade-off for these parameters
272 determined by Fei (1996) for B1-FeO, whose preferred values were 149 GPa and 3.5.
273 Isotherms calculated from our equation of state of B1-FeO are shown in Figure 2. We
274 find that K_0' must be less than four to fit the higher-pressure data, which explains the

misfit between these data and the extrapolated equation of state of Campbell et al. (2009), who fixed K_0' to 4.0 in their analysis.

For B8-FeO, we fit the present data along with those of Ozawa et al. (2010). This phase is not recoverable to ambient conditions, so V_0 is a fitted parameter, and a reduction in the number of other fitted parameters was achieved by fixing $K_0' = 4$ and $q = 1$ and assuming the Debye temperature to be equal to that of B1-FeO (Stixrude and Lithgow-Bertelloni, 2007). It was necessary to hold these parameters fixed due to the limited *P-T* range of the B8 data, and as a consequence, this equation of state should not be extrapolated far outside the range of the data. The zero-pressure volume V_0 for B8-FeO was found to be 2.1% smaller than that of B1-FeO (McCammon and Liu, 1984) (Table 1). We found a lower value of K_0 for B8-FeO than for B1-FeO (137.8 GPa *vs.* 149.4 GPa), but we used a higher value of K_0' for the B8 phase, so it is less compressible at the high pressure conditions under which it exists. We also found different values of γ_0 for the two phases, but their γ become very similar at high pressures due to the different q values in the fits. Isotherms calculated from our equation of state of B8-FeO are shown in Figure 3. There is significant misfit between our equation of state and the data points of Fei and Mao (1994) and Kondo et al. (2004). Both of these studies used non-stoichiometric wüstite, while this study and Ozawa et al. (2010) used iron-saturated FeO, but stoichiometric effects should cause the data of Fei and Mao (1994) and Kondo et al. (2004) to be shifted to smaller volumes of wüstite, whereas their data have larger volumes than are predicted by our equation of state (Figure 3). The cause of this discrepancy is unknown, though it could have the same underlying basis as the disagreement over the B1/B8 phase boundary between our data and those of Fei and Mao

298 (1994) (Section 4.1). The data point of Kondo et al. (2004) does agree with our equation
299 of state within its large pressure uncertainty, but the misfit should be greater taking into
300 account the effects of stoichiometry.
301
302 *4.3. Core density deficit*
303 We can use the knowledge that wüstite is stable in the B1 structure under the *P-T*
304 conditions of the Earth's core (Section 4.1) and our improved equation of state for B1-
305 FeO at core conditions (Section 4.2) to evaluate the core density deficit. Several
306 assumptions are required for this analysis. We assume the pressure at the core-mantle
307 boundary (CMB) to be 135.8 GPa (Dziewonski and Anderson, 1981), and we use an
308 outer core temperature of 4000 ± 500 K at the CMB based on the analysis of Anderson
309 (2003). We also assume that the outer core is convecting near adiabatic conditions (Birch,
310 1952), and that iron and iron-rich alloys experience a 1-2% volume increase upon melting
311 at core pressures (Anderson, 2003). Although it is likely that the outer core contains
312 significant amounts of more than one light element, including O, S, Si, and/or C
313 (McDonough, 2003), in this analysis we consider an outer core whose light element
314 component is purely oxygen.
315 Figure 5 illustrates the density difference between pure iron (Dewaele et al.,
316 2006), calculated along an adiabat, and a seismologically-determined density profile of
317 the Earth's core, the Preliminary Reference Earth Model (PREM) (Dziewonski and
318 Anderson, 1981). Using the assumptions described above, we find that PREM is 10.4 ±
319 0.9% less dense than solid hcp-iron at the core-mantle boundary. Approximately 1-2% of
320 this density difference can be accounted for by the ΔV of melting of iron (Anderson,

2003), but the remainder must be due to the presence of one or more light elements in the core, such as oxygen.

Our equation of state for B1-FeO can be used to place firm constraints on the amount of oxygen in Earth's core, because it requires no extrapolation in pressure and only a small extrapolation in temperature to be applied at the *P-T* conditions of the CMB. For a core model containing only iron and oxygen, we find that 7.7 ± 1.1 weight percent oxygen would be required in the outer core to match PREM at the core-mantle boundary. Allowing for the presence of nickel in the core slightly alters this result. Correcting the outer core density to account for a Ni/Fe atomic ratio of 0.058 in the core (McDonough, 2003), we find that 7.9 ± 1.1 weight percent oxygen would be necessary to match PREM at the CMB for an Fe-Ni-O core.

Figure 5 shows that the slopes of the adiabatic density profiles of hcp-Fe and B1-FeO do not exactly match that of PREM when these equations of state are extrapolated over the *P-T* range of the Earth's core. Their slopes also do not match each other, due to the K_0' value for FeO being smaller than that of iron (3.60 *vs.* 5.38) (Dewaele et al., 2006). For this reason, we have limited our calculations of the core density deficit to the core-mantle boundary, minimizing extrapolation. If oxygen is the dominant light element in the core, these differences in curvature could be due to several factors, including: PREM not accurately describing the precise density variations through the core; the need for an additional term in these equations of state when extrapolating them to such high pressures and temperatures; a compositional gradient through the outer core; a more complex mixing relationship between Fe and FeO at these conditions; or the presence of one or more other light elements.

344

345 *4.4. Oxygen fugacity buffer*

346 Oxygen fugacity (fO_2) governs many key physical and chemical properties of
347 minerals, including insulator-metal transitions, diffusion rates, rheological properties, and
348 elemental partitioning. The fO_2 of the Earth's interior is dominated by the valence state of
349 iron, the most abundant multivalent element in the planet. Therefore it is critical to
350 understand the Fe-FeO oxygen fugacity buffer at pressures and temperatures relevant to
351 the deep Earth. In this study we have extended the equation of state of B1-FeO to higher
352 *P-T* conditions, allowing us to extend calculations of the Fe-FeO fO_2 buffer to these more
353 extreme conditions.

354 We have calculated this buffer by comparing the equations of state of B1-FeO
355 (Section 4.2), fcc-Fe (Campbell et al., 2009), and hcp-Fe (Dewaele et al., 2006),
356 following the method of Campbell et al. (2009):

357 $$\log fO_2 = \log fO_2(1\text{bar}) + (0.8686/RT) \int \Delta V \mathrm{d}P \quad (2)$$

358 where ΔV is the volume difference between FeO and iron. The calculated buffer is strictly
359 applicable only for FeO in the B1 structure, and only for high-spin FeO. Iron-poor
360 (Mg,Fe)O in the Earth's lower mantle may undergo a spin transition to the low-spin state
361 (Cohen et al., 1997; Lin et al., 2005), which will likely have a significant effect on the Fe-
362 FeO oxygen fugacity buffer.

363 The calculated fO_2 buffers are shown in Figure 6, and tabulated values at smaller
364 pressure increments are shown in Table S2 of the Supplementary Material. The results
365 found here are similar to those presented in Campbell et al. (2009), with the buffers
366 calculated in this study differing from those of Campbell et al. (2009) by less than 0.2 log

367 units up to 100 GPa, the highest pressure shown by Campbell et al. (2009). However, this
368 discrepancy increases with pressure, becoming larger at the higher pressures achieved in
369 this study. We confirm the results of Campbell et al. (2009) that the absolute fO_2
370 values increase with pressure at each temperature, and that the slope $\partial(\ln fO_2)/\partial T|_P$
371 decreases with pressure, eventually becoming a slope of approximately zero at 60 GPa
372 and negative at higher pressures. Also included in Table S2 is a polynomial expression of
373 the Fe-FeO buffer as a function of pressure and temperature, which can be used as a
374 convenience to interpolate between the tabulated values.

375 The oxygen fugacity buffers calculated in this section are specifically for
376 stoichiometric FeO, because that is the endmember component in the important
377 applications to high-pressure mineral physics and the chemistry of the Earth's mantle. In
378 applications where FeO-bearing silicates or oxides exist with Fe-bearing metal, the
379 oxygen fugacity of a system can be determined relative to the Fe-FeO buffer. Near
380 ambient pressure, nonstoichiometric wüstite is the stable oxide that coexists with metallic
381 iron, so the iron-wüstite buffer is frequently applied with respect to these
382 nonstoichiometric oxides, especially when this solid state buffer is used directly to
383 control the oxygen fugacity in low-pressure experiments. However, above several GPa,
384 stoichiometric FeO becomes stable in the presence of Fe (Campbell et al., 2009; Seagle et
385 al., 2008; Stølen and Grønvold, 1996), so even when used directly to buffer a system, it is
386 the Fe-FeO reaction that is relevant.

387 Nevertheless, it is interesting to consider whether nonstoichiometric wüstite
388 becomes stable again at high pressures when coexisting with metallic Fe. The relevant
389 reaction is $Fe_{1-x}O + xFe \rightleftarrows FeO$, and the pressure dependence of this reaction is

390 determined by the volume difference V(FeO) - V($Fe_{1-x}O$) - xV(Fe). The present study
391 provides the equation of state of FeO, and equations of state exist for both fcc and hcp
392 phases of Fe (e.g., Campbell et al., 2009; Dewaele et al., 2006), but the equations of state
393 of wüstites are not precisely determined over the P-T range of interest. However, it has
394 been concluded by Fei (1996) that the bulk modulus of $Fe_{1-x}O$ is constant for all x; if we
395 suppose for purposes of this calculation that all other thermoelastic parameters are also
396 independent of x, then we can evaluate the equation of state for any wüstite based on the
397 equation of state parameters for FeO in this study (Table 1) and the zero-pressure lattice
398 parameters of McCammon and Liu (1984). Our results of this calculation show that for
399 all values of x, the volume change V(FeO) - V($Fe_{1-x}O$) - xV(Fe) is negative over all
400 conditions calculated (0 to 200 GPa; 300 to 2500 K). Therefore, stoichiometric FeO, and
401 not nonstoichiometric wüstite, remains the stable oxide coexisting with Fe at all high P-T
402 conditions above the several GPa range as reported by Stølen and Grønvold (1996).
403
404
405 **5. Conclusions**
406
407 The phase diagram of stoichiometric FeO, and the equations of state of its B1 and
408 B8 structures, were measured to high temperatures and pressures reaching those of the
409 Earth's outer core. The positive slope for the phase boundary between the subsolidus B1
410 and B8 phases of FeO is broadly consistent with those reported by Kondo et al. (2004)
411 and Ozawa et al. (2010). These results confirm that the stable phase of FeO at conditions
412 of the Earth's deep interior has the B1 structure, not the B8 structure. The equation of

413 state of B1-FeO reported by Campbell et al. (2009) did not precisely describe these new
414 higher pressure data, but the updated equation of state presented here accurately describes
415 not only our new data but also those of several previous studies (Campbell et al., 2009;
416 Ozawa et al., 2010; Seagle et al., 2008). We also combined our data with those of Ozawa
417 et al. (2010) to construct an equation of state for B8-FeO.

418 Using our improved equation of state for B1-FeO and earlier equations of state for
419 fcc- and hcp-Fe (Campbell et al., 2009; Dewaele et al., 2006), we have recalculated high-
420 pressure, high-temperature Fe-FeO oxygen fugacity buffers, improving the accuracy of
421 these buffers over those reported by Campbell et al. (2009) at pressures >100 GPa. The
422 equation of state for B1-FeO can be compared to that of hcp-Fe (Dewaele et al., 2006)
423 and the seismologically determined density of the Earth's core (Dziewonski and
424 Anderson, 1981), to analyze the core density deficit. For a core composition in which
425 oxygen is the sole light element, 7.9 ± 1.1 weight percent oxygen would be required in
426 the outer core to match PREM at the core-mantle boundary.
427

Acknowledgments

Portions of this work were performed at GeoSoilEnviroCARS (Sector 13), Advanced Photon Source (APS), Argonne National Laboratory. GeoSoilEnviroCARS is supported by the National Science Foundation - Earth Sciences (EAR-0622171) and Department of Energy - Geosciences (DE-FG02-94ER14466). Use of the Advanced Photon Source was supported by the U. S. Department of Energy, Office of Science, Office of Basic Energy Sciences, under Contract No. DE-AC02-06CH11357. We thank the anonymous reviewers for constructive comments. This work was supported by the National Science Foundation by grant EAR 0847217 to A.J.C.

438 **References**

439

440 Anderson, O.L., 2003. The three-dimensional phase diagram of iron, in: Dehant, V.,
441 Creager, K.C., Karato, S.-i., Zatman, S. (Eds.), Earth's Core: Dynamics,
442 Structure, Rotation. American Geophysical Union, Washington, DC, pp. 83-103.
443 Anderson, O.L., Isaak, D.G., Yamamoto, S., 1989. Anharmonicity and the equation of
444 state for gold. J. Appl. Phys. 65, 1534-1543.
445 Birch, F., 1952. Elasticity and constitution of the Earth's interior. J. Geophys. Res. 37,
446 227-286.
447 Boehler, R., 1992. Melting of the Fe-FeO and the Fe-FeS systems at high pressure –
448 constraints on core temperatures. Earth Planet. Sci. Lett. 111, 217-227.
449 Boehler, R., 1996. Melting temperature of the Earth's mantle and core: Earth's thermal
450 structure. Annu. Rev. Earth Planet. Sci. 24, 15-40.
451 Campbell, A.J., Seagle, C.T., Heinz, D.L., Shen, G., Prakapenka, V.B., 2007. Partial
452 melting in the iron-sulfur system at high pressure: A synchrotron X-ray
453 diffraction study. Phys. Earth Planet. Inter. 162, 119-128.
454 Campbell, A.J., Danielson, L., Righter, K., Seagle, C.T., Wang, Y., Prakapenka, V.B.,
455 2009. High pressure effects on the iron-iron oxide and nickel-nickel oxide oxygen
456 fugacity buffers. Earth Planet. Sci. Lett. 286, 556-564.
457 Chase Jr., M.W., 1998. NIST-JANAF Thermochemical Tables, 4th ed. : J. Phys. Chem.
458 Ref. Data Monograph No. 9. American Institute of Physics.
459 Cohen, R.E., Mazin, I.I., Isaak, D.G., 1997. Magnetic collapse in transition metal oxides
460 at high pressure: Implications for the Earth. Science 275, 654-657.

461 Dewaele, A., Loubeyre, P., Occelli, F., Mezouar, M., Dorogokupets, P.I., Torrent, M.,
462 2006. Quasihydrostatic equation of state of iron above 2 Mbar. Phys. Rev. Lett.
463 97, 215504.
464 Dziewonski, A.M., Anderson, D.L., 1981. Preliminary reference Earth model. Phys.
465 Earth Planet. Inter. 25, 297-356.
466 Fei, Y., 1996. Crystal chemistry of FeO at high pressure and temperature, in: Dyar, M.D.,
467 McCammon, C., Schaefer, M.W. (Eds.), Mineral Spectroscopy: A Tribute to
468 Roger G. Burns. The Geochemical Society, Houston, pp. 243-254.
469 Fei, Y., Mao, H.-k., 1994. In-situ determination of the NiAs phase of FeO at high-
470 pressure and temperature. Science 266, 1678-1680.
471 Fischer, R.A., Campbell, A.J., 2010. High pressure melting of wüstite. Am. Mineral. 95,
472 1473-1477.
473 Fjellvåg, H., Hauback, B.C., Vogt, T., Stølen, S., 2002. Monoclinic nearly stoichiometric
474 wüstite at low temperatures. Am. Mineral. 87, 347-349.
475 Frost, D.J., McCammon, C.A., 2008. The redox state of Earth's mantle. Annu. Rev. Earth
476 Planet. Sci. 36, 389-420.
477 Hammersley, A.P., Svensson, S.O., Hanfland, M., Fitch, A.N., Hausermann, D., 1996.
478 Two-dimensional detector software: From real detector to idealized image or two-
479 theta scan. High Press. Res. 14, 235-248.
480 Heinz, D.L., Jeanloz, R., 1987. Temperature measurements in the laser-heated diamond
481 cell, in: Manghnani, M.H., Syono, Y. (Eds.), High-Pressure Research in Mineral
482 Physics. Terra Scientific Publishing, Tokyo / American Geophysical Union,
483 Washington, pp. 113-127.

484 Jeanloz, R., Ahrens, T.J., 1980. Equations of state of FeO and CaO. Geophys. J. R. astr.
485 Soc. 62, 505-528.
486 Kantor, I., Kurnosov, A., McCammon, C., Dubrovinsky, L., 2008. Monoclinic FeO at
487 high pressures. Z. Krist. 223, 461-464.
488 Knittle, E., Jeanloz, R., 1991. The high-pressure phase diagram of $Fe_{0.94}O$: A possible
489 constituent of the Earth's core. J. Geophys. Res. 96, 16169-16180.
490 Komabayashi, T., Fei, Y., 2010. Internally consistent thermodynamic database for iron to
491 the Earth's core conditions. J. Geophys. Res. 115, B03202.
492 Kondo, T., Ohtani, E., Hirao, N., Yagi, T., Kikegawa, T., 2004. Phase transitions of
493 (Mg,Fe)O at megabar pressures. Phys. Earth Planet. Inter. 143-144, 201-213.
494 Lin, J.-F., Struzhkin, V.V., Jacobsen, S.D., Hu, M.Y., Chow, P., Kung, J., Liu, H., Mao,
495 H.-k., Hemley, R.J., 2005. Spin transition of iron in magnesiowüstite in the
496 Earth's lower mantle. Nature 436, 377-380.
497 Mao, H.-k., Bell, P.M., Shaner, J.W., Steinberg, D.J., 1978. Specific volume
498 measurements of Cu, Mo, Pd, and Ag and calibration of the ruby R_1 fluorescence
499 pressure gauge from 0.06 to 1 Mbar. J. Appl. Phys. 49, 3276-3283.
500 Mao, H.-k., Shu, J., Fei, Y., Hu, J., Hemley, R.J., 1996. The wüstite enigma. Phys. Earth
501 Planet. Inter. 96, 135-145.
502 McCammon, C., 1993. Effect of pressure on the composition of the lower mantle end
503 member Fe_xO. Science 259, 66-68.
504 McCammon, C.A., Liu, L.-G., 1984. The effects of pressure and temperature on non-
505 stoichiometric wüstite, Fe_xO: The iron-rich phase boundary. Phys. Chem. Miner.
506 10, 106-113.

McDonough, W.F., 2003. Compositional model for the Earth's core, in: Carlson, R.W. (Ed.), Treatise of Geochemistry, Vol. 2. Elsevier-Pergamon, Oxford, pp. 547-568.

Murakami, M., Hirose, K., Ono, S., Tsuchiya, T., Isshiki, M., Watanuki, T., 2004. High pressure and high temperature phase transitions of FeO. Phys. Earth Planet. Inter. 146, 273-282.

Ozawa, H., Hirose, K., Tateno, S., Sata, N., Ohishi, Y., 2010. Phase transition boundary between B1 and B8 structures of FeO up to 210 GPa. Phys. Earth Planet. Inter. 179, 157-163.

Prakapenka, V.B., Kuba, A., Kuznetsov, A., Laskin, A., Shkurikhin, O., Dera, P., Rivers, M.L., Sutton, S.R., 2008. Advanced flat top laser heating system for high pressure research at GSECARS: Application to the melting behavior of germanium. High Press. Res. 28, 225-235.

Ringwood, A.E., Hibberson, W., 1990. The system Fe-FeO revisited. Phys. Chem. Miner. 17, 313-319.

Sata, N., Hirose, K., Oshino, Y., Shen, G., 2005. High-pressure experiments on FeO up to 200 GPa. EOS Trans. AGU 86, Fall Meet. Suppl., Abstract MR31A-0124.

Seagle, C.T., Heinz, D.L., Campbell, A.J., Prakapenka, V.B., Wanless, S.T., 2008. Melting and thermal expansion in the Fe-FeO system at high pressure. Earth Planet. Sci. Lett. 265, 655-665.

Shen, G., Lazor, P., Saxena, S.K., 1993. Melting of wüstite and iron up to pressures of 600 kbar. Phys. Chem. Minerals 20, 91-96.

Shen, G., Mao, H.-K., Hemley, R.J., Duffy, T.S., Rivers, M.L., 1998. Melting and crystal structure of iron at high pressures. Geophys. Res. Lett. 25, 373–376.

Shen, G.Y., River, M.L., Wang, Y.B., Sutton, S.R., 2001. Laser heated diamond anvil cell system at the Advanced Photon Source for in situ x-ray measurements at high pressure and temperature. Rev. Sci. Instrum. 72, 1273-1282.

Shen, G., Rivers, M.L., Wang, Y., Sutton, S.R., 2005. Facilities for high-pressure research with the diamond anvil cell at GSECARS. J. Synchrotron Rad. 12, 642-649.

Stixrude, L., Lithgow-Bertelloni, C., 2007. Influence of phase transformations on lateral heterogeneity and dynamics in Earth's mantle. Earth Planet. Sci. Lett. 263, 45-55.

Stølen, S., Grønvold, F., 1996. Calculation of the phase boundaries of wüstite at high pressure. J. Geophys. Res. 101, 11531–11540.

Yagi, T., Suzuki, K., Akimoto, S., 1985. Static compression of wüstite ($Fe_{0.98}O$) to 120 GPa. J. Geophys. Res. 90, 8784-8788.

Yagi, T., Fukuoka, K., Takei, H., Syono, Y., 1988. Shock compression of wüstite. Geophys. Res. Lett. 15, 816-819.

Zen, E.-A.,1966. Construction and pressure-temperature diagrams for multicomponent systems after the method of Schreinemakers geometric approach. U.S. Geological Survey Bulletin 1225.

Figure Captions

Figure 1. a: Diffraction image before integration, collected at 144 GPa and 3025 K. b: Diffraction pattern from part A integrated azimuthally. Peaks correspond to B2-NaCl, B1-FeO, and hcp-Fe. c: Diffraction pattern collected at 151 GPa and 1665 K, integrated azimuthally, with peaks corresponding to B2-NaCl, B8-FeO, and hcp-Fe.

Figure 2. Equation of state of B1-FeO. Filled circles: this study. Open triangles: Ozawa et al. (2010). Open squares: Seagle et al. (2008). Open diamonds: Campbell et al. (2009). All data and isotherms are color-coded by temperature range according to the legend. Isotherms are calculated using the parameters in Table 1 for the midpoint of the temperature range indicated, and they do not extend above the melting curve of Fischer and Campbell (2010).

Figure 3. Equation of state of B8-FeO. Filled circles: this study. Open triangles: Ozawa et al. (2010). ×: Kondo et al. (2004). Cross: Fei and Mao (1994). Errors in volume from this study were fixed at ± 0.1 cm^3/mol when they could not be constrained by the data. Fei and Mao (1994) do not report an error in pressure. All data and isotherms are color-coded by temperature range, as in Figure 2. Isotherms are calculated using the parameters in Table 1 for the midpoint of the temperature range indicated, and they do not extend above the melting curve of Fischer and Campbell (2010).

Figure 4. High *P-T* phase diagram of wüstite. Pink symbols: stability field of B8 (NiAs-type) FeO. Blue symbols: stability field of B1 (NaCl-type) FeO. Filled circles: this study. ×: Kondo et al. (2004). Open triangles: Ozawa et al. (2010). Brown lines: phase boundaries of rhombally-distorted wüstite (Fei and Mao, 1994). Black line: melting curve from Fischer and Campbell (2010), extrapolated (dashed line) using Lindemann melting law. Gray: approximate geotherm, after Boehler (1996). This study and Ozawa et al. (2010) report phase stability of stoichiometric FeO, while Kondo et al (2004) used $Fe_{0.95}O$, Fei and Mao (1994) used $Fe_{0.98}O$, and Fischer and Campbell (2010) used $Fe_{0.94}O$.

Figure 5. Core density deficit. Grey line: PREM (Dziewonski and Anderson, 1981). Blue line: density profile for B1-FeO, calculated from the parameters listed in Table 1. Orange line: density profile for hcp-Fe, calculated from the equation of state of Dewaele et al. (2006). Solid lines follow an adiabatic temperature profile for a CMB temperature of 4000 K. Dashed lines indicate the effect of a ± 500 K uncertainty in the CMB temperature.

Figure 6. Fe–FeO oxygen fugacity buffers at high pressures and temperatures. The 1 bar buffer curve was calculated from Chase (1998), and high pressure curves were calculated from Eq. (2) using fits to the data like those in Figure 2. These buffers are only valid for B1-FeO in the high-spin state.

592 **Table 1.** Equation of state parameters for B1- and B8-FeO.

593

	B1-FeO	B8-FeO
V_0 (cm^3/mol)	*12.256*[a]	11.997 ± 0.018
K_0 (GPa)	149.4 ± 1.0	137.8 ± 0.9
K_0'	3.60 ± 0.04	*4*
θ_0 (K)	*417*[b]	*417*[b]
γ_0	1.41 ± 0.05	1.73 ± 0.12
q	*0.5*	*1*

Entries in italics were held fixed in the fit.
[a]McCammon and Liu (1984)
[b]Stixrude and Lithgow-Bertelloni (2007)

594

595

596

Supplementary Material

Supplementary Table S1. Pressure-volume-temperature data from synchrotron X-ray diffraction experiments. Pressures are determined from the unit cell volumes of hcp-Fe using the equation of state of Dewaele et al. (2006). Reported temperatures are corrected for an axial temperature gradient.

Supplementary Table S2. Tabulation of the Fe-FeO oxygen fugacity buffer at high pressures and temperatures.

Figure 1a

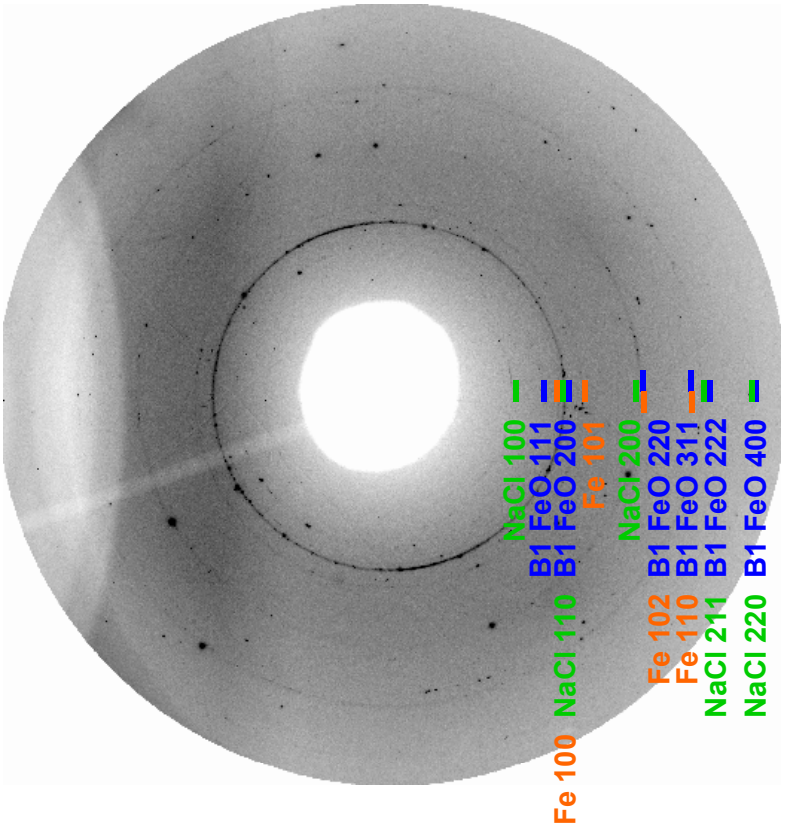

Figure 1b

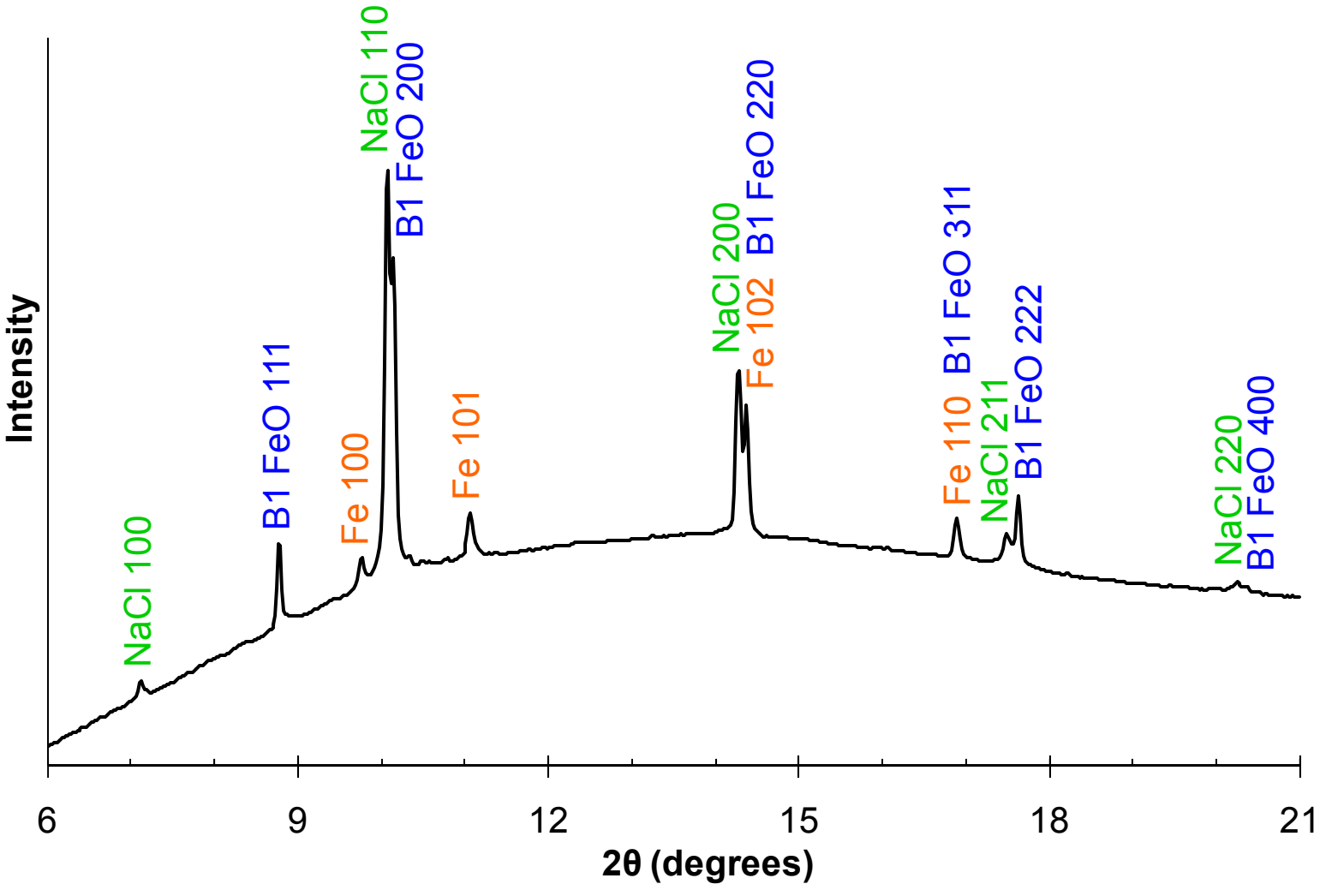

Figure 1c

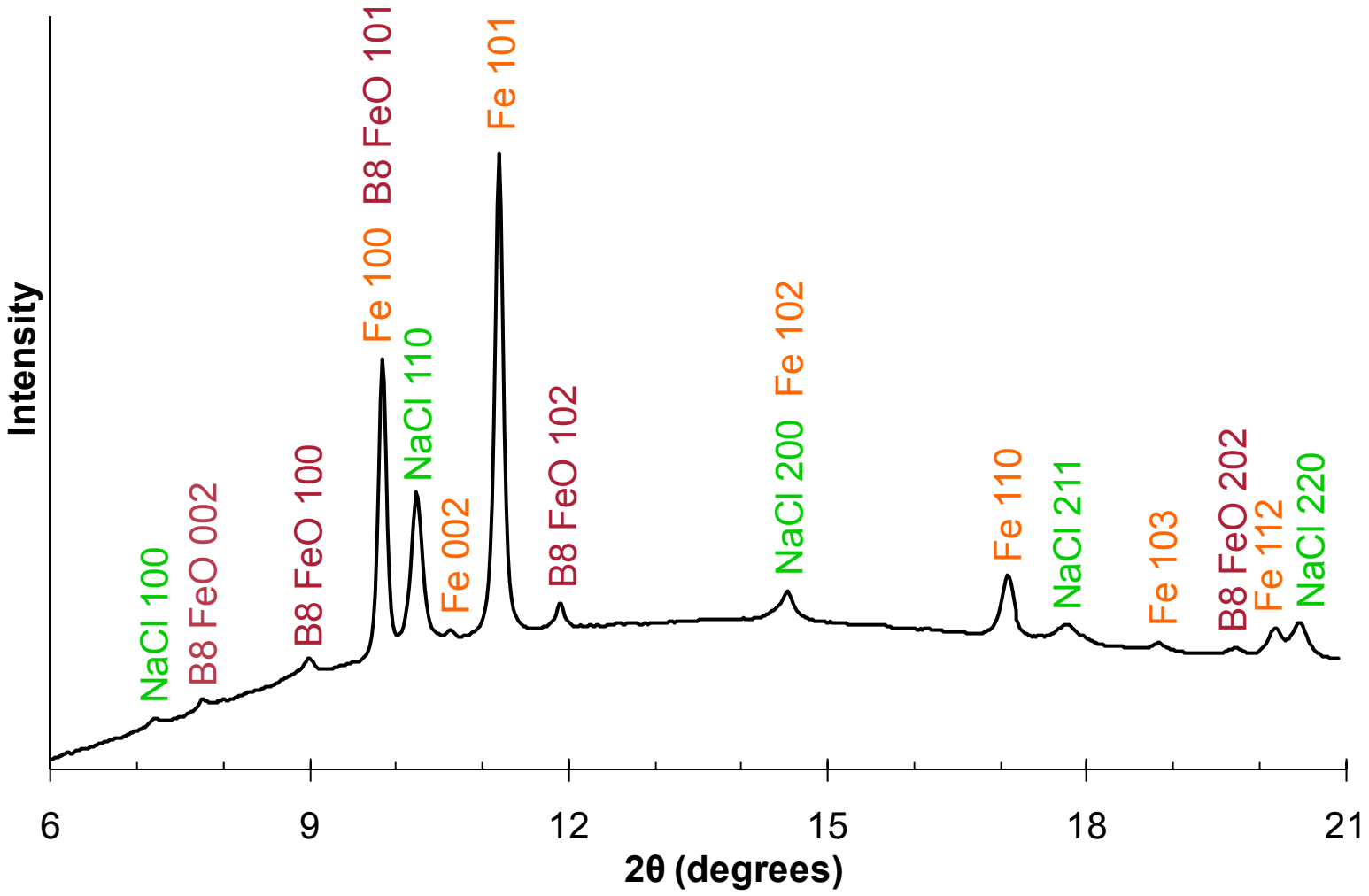
Intensity
NaCl 100
B8 FeO 002
B8 FeO 100
Fe 100
B8 FeO 101
NaCl 110
Fe 002
Fe 101
B8 FeO 102
NaCl 200
Fe 102
Fe 110
NaCl 211
Fe 103
B8 FeO 202
Fe 112
NaCl 220
6
9
12
15
18
21
2θ (degrees)

Figure 2

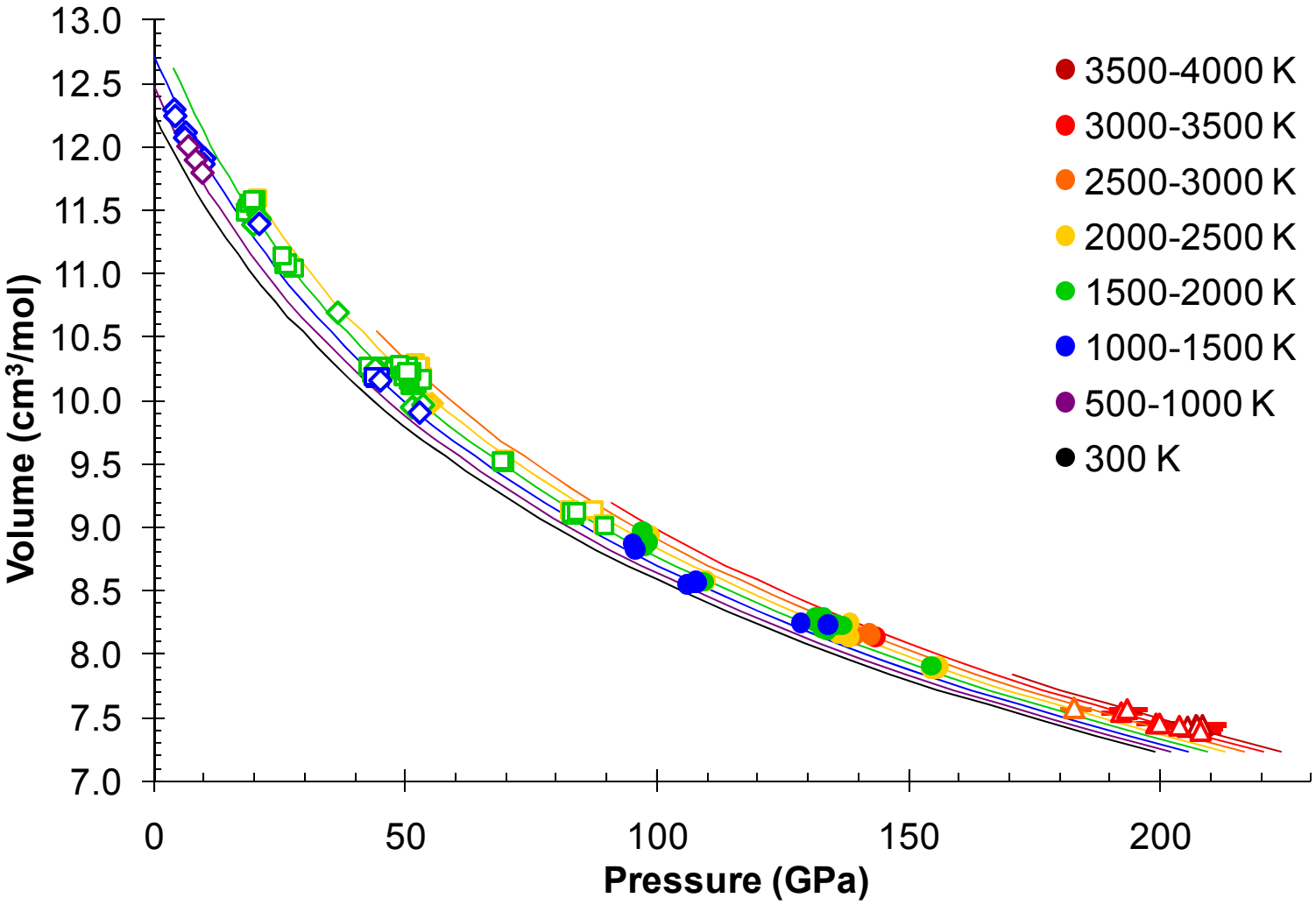
13.0
12.5
12.0
11.5
11.0
10.5
10.0
9.5
9.0
8.5
8.0
7.5
7.0
Volume (cm³/mol)
0
50
100
150
200
Pressure (GPa)
3500-4000 K
3000-3500 K
2500-3000 K
2000-2500 K
1500-2000 K
1000-1500 K
500-1000 K
300 K

Figure 3

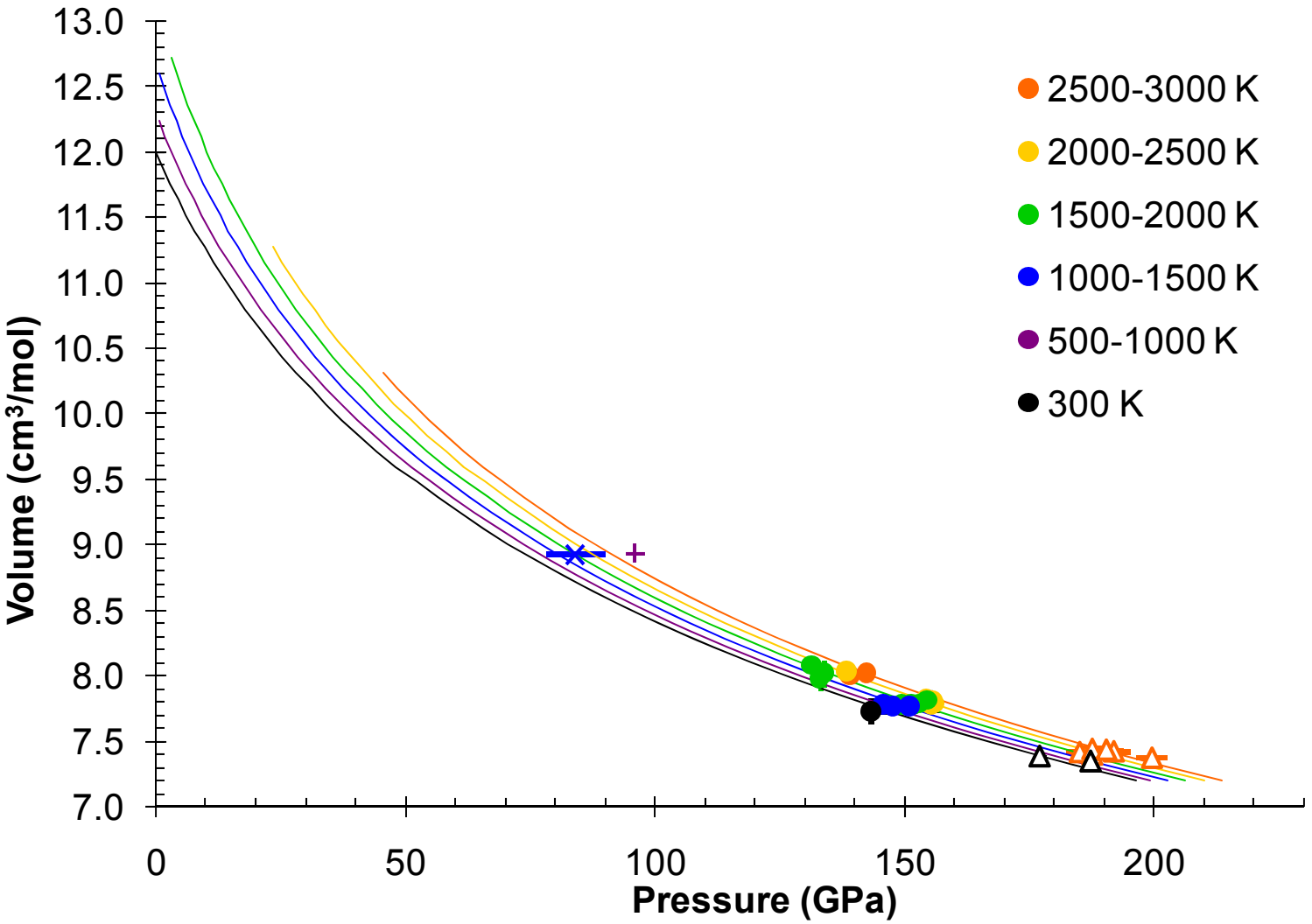
13.0
12.5
12.0
11.5
11.0
10.5
10.0
9.5
9.0
8.5
8.0
7.5
7.0
Volume (cm³/mol)
0
50
100
150
200
Pressure (GPa)
2500-3000 K
2000-2500 K
1500-2000 K
1000-1500 K
500-1000 K
300 K

Figure 4

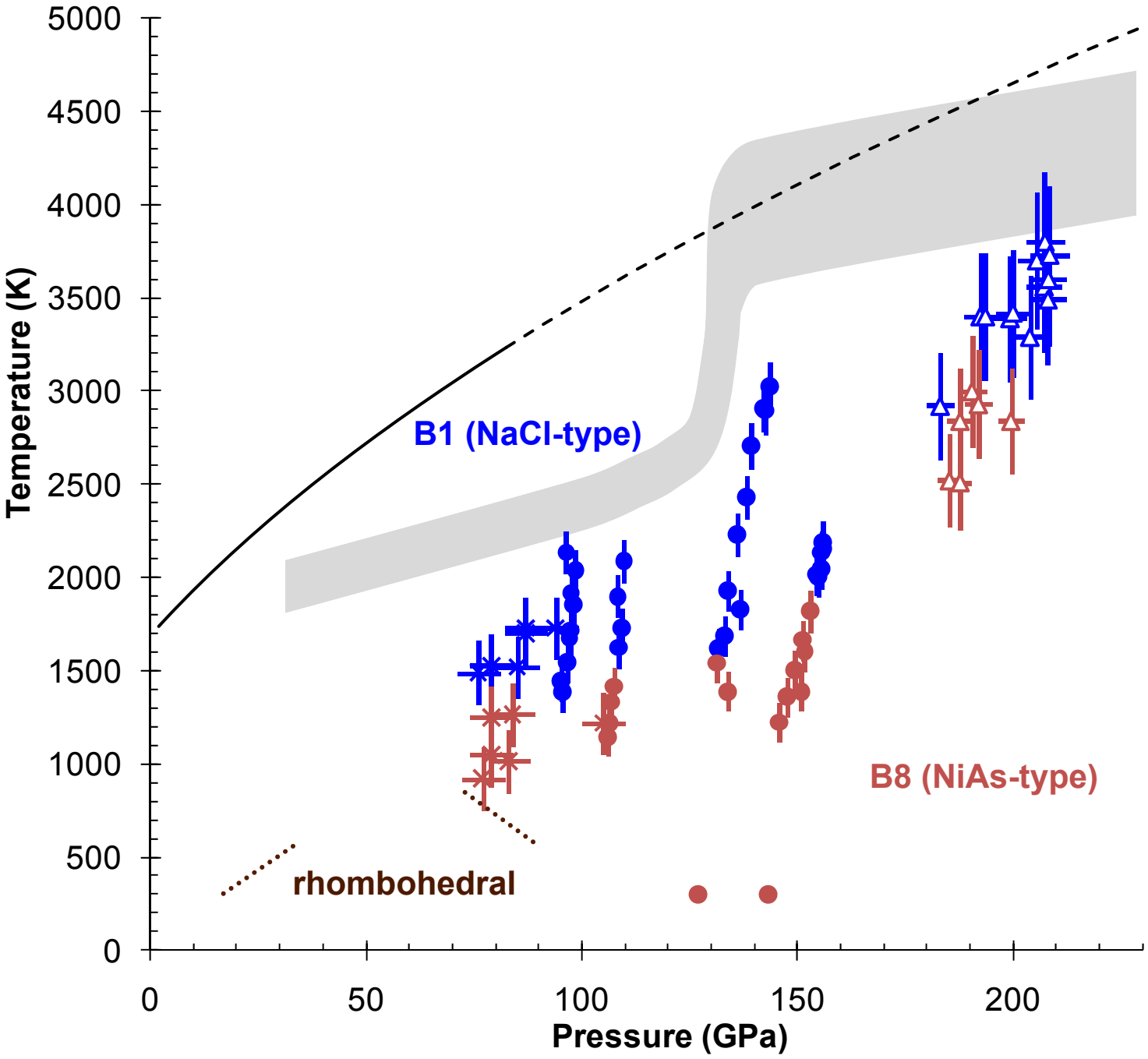
5000
4500
4000
3500
3000
2500
2000
1500
1000
500
0
Temperature (K)
0
50
100
150
200
Pressure (GPa)
B1 (NaCl-type)
B8 (NiAs-type)
rhombohedral

Figure 5

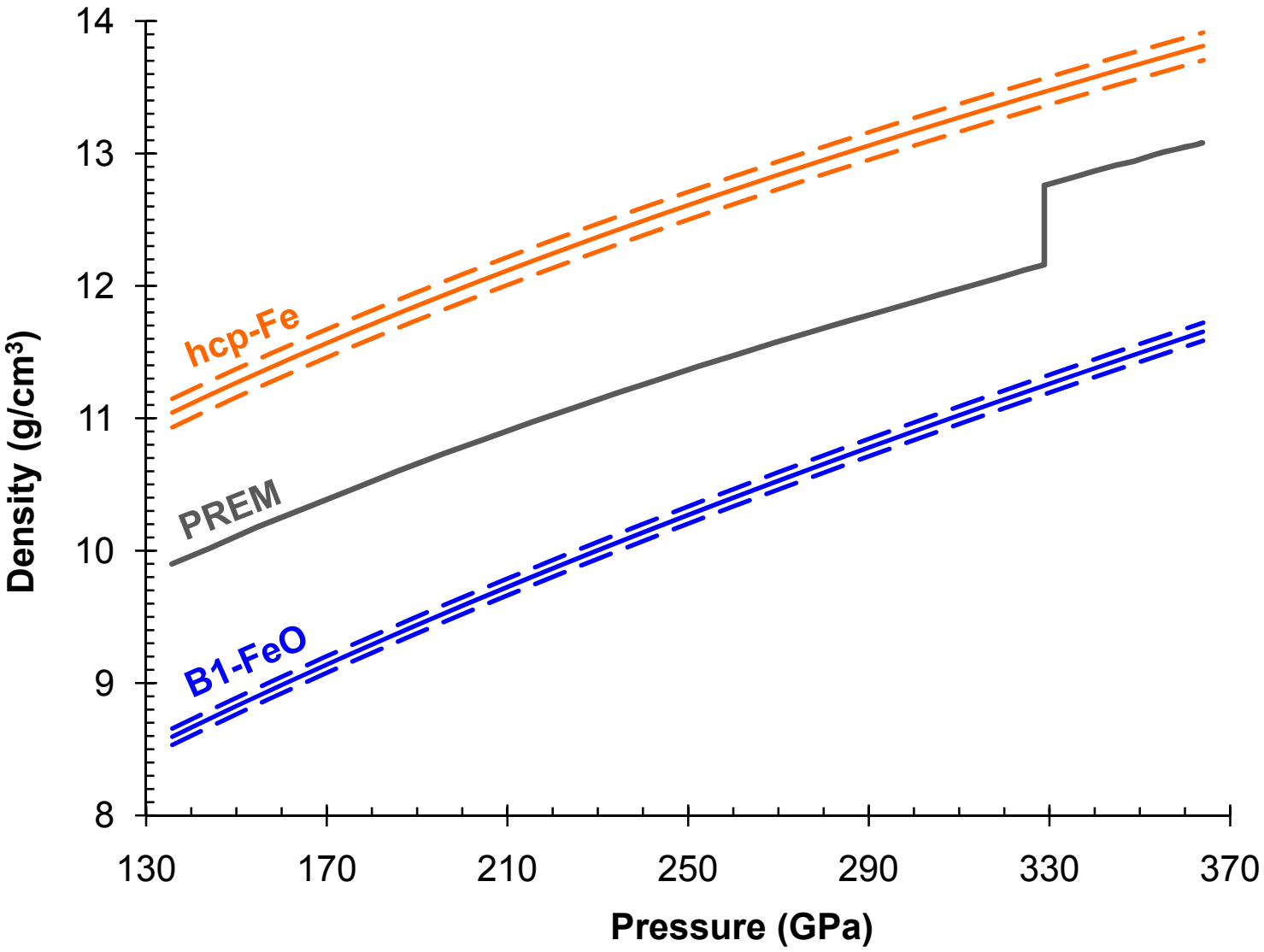
14
13
12
11
10
9
8
Density (g/cm³)
hcp-Fe
PREM
B1-FeO
130
170
210
250
290
330
370
Pressure (GPa)

Figure 6

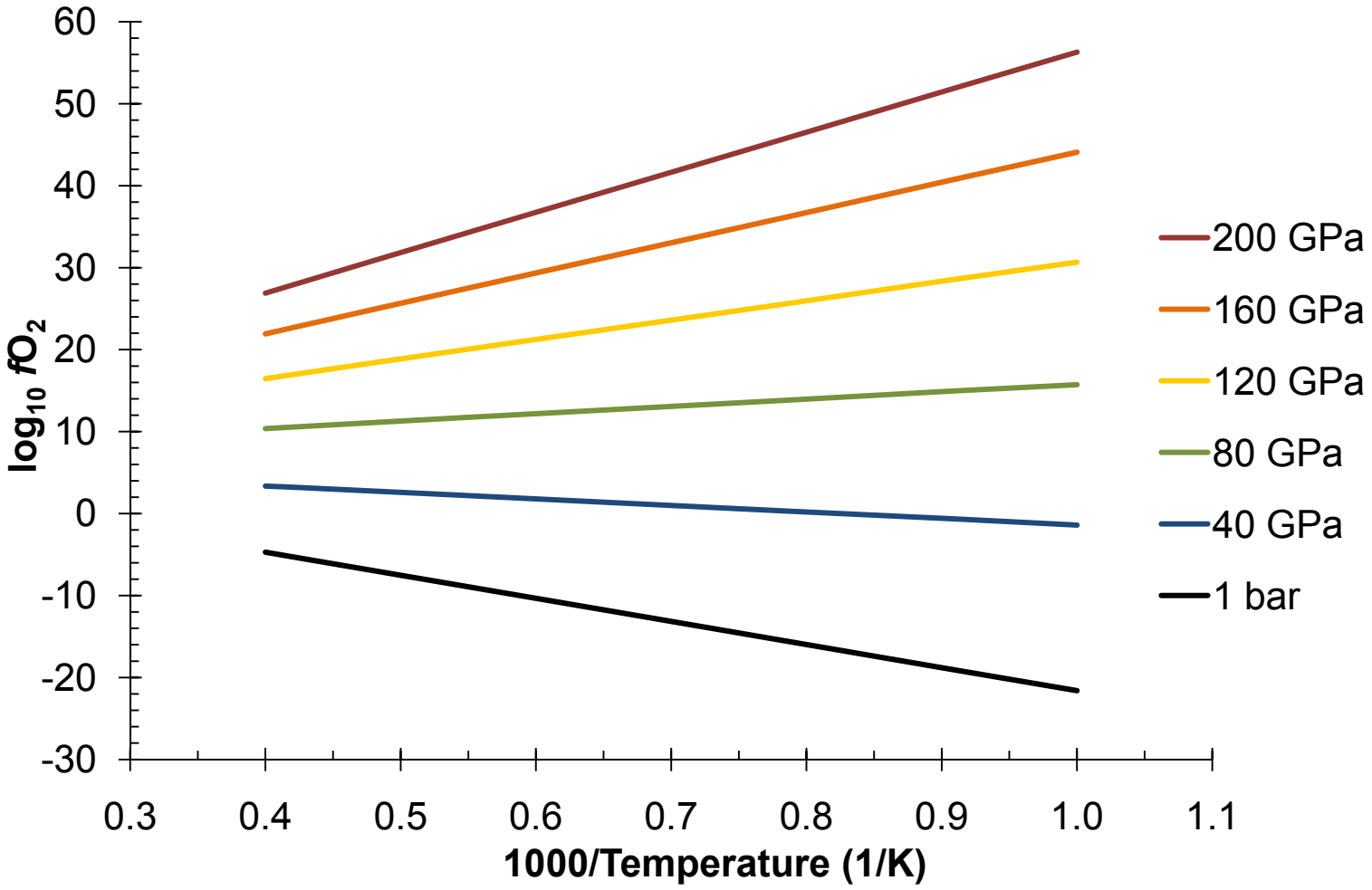
60
50
40
30
20
10
0
-10
-20
-30
log10 fO2
0.3
0.4
0.5
0.6
0.7
0.8
0.9
1.0
1.1
1000/Temperature (1/K)
200 GPa
160 GPa
120 GPa
80 GPa
40 GPa
1 bar